Wearable Microfluidic Diaphragm Pressure Sensor for Health and Tactile Touch Monitoring

Yuji Gao, Hiroki Ota, Ethan W. Schaler, Kevin Chen, Allan Zhao, Wei Gao, Hossain M. Fahad, Yonggang Leng, Anzong Zheng, Furui Xiong, Chuchu Zhang, Li-Chia Tai, Peida Zhao, Ronald S. Fearing, and Ali Javey*

Dr. Y. Gao, Dr. H. Ota, Dr. E. W. Schaler, Dr. K. Chen, A. Zhao, Dr. W. Gao, Dr. H. M. Fahad, C. Zhang, L.-C. Tai, P. Zhao, Prof. R. S. Fearing, Prof. A. Javey: Department of Electrical Engineering and Computer Sciences University of California Berkeley, CA 94720, USA E-mail: ajavey@eecs.berkeley.edu; Dr. Y. Gao, Dr. H. Ota, Dr. K. Chen, Dr. W. Gao, Dr. H. M. Fahad, Prof. A. Javey: Berkeley Sensor and Actuator Center, University of California Berkeley, CA 94720, USA; Dr. Y. Gao, Dr. H. Ota, Dr. K. Chen, Dr. W. Gao, L.-C. Tai, P. Zhao, Prof. A. Javey: Materials Sciences Division, Lawrence Berkeley National Laboratory, Berkeley, CA 94720, USA; Dr. Y. Gao, Prof. Y. Leng, Dr. F. Xiong: School of Mechanical Engineering, Tianjin University, Tianjin 300072, China; Prof. Y. Leng: Key Laboratory of Mechanism Theory and Equipment Design of Ministry of Education, Tianjin University, Tianjin 300072, China; A. Zheng: National Center for Computer Animation, Bournemouth University, Bournemouth BH12 5BB, UK

Abstract

Flexible pressure sensors have many potential applications in wearable electronics, robotics, health monitoring, and more. In particular, liquid-metal-based sensors are especially promising as they can undergo strains of over 200% without failure. However, current liquid-metal-based strain sensors are incapable of resolving small pressure changes in the few kPa range, making them unsuitable for applications such as heart-rate monitoring, which require a much lower pressure detection resolution. In this paper, a microfluidic tactile diaphragm pressure sensor based on embedded Galinstan microchannels (70 μm width × 70 μm height) capable of resolving sub-50 Pa changes in pressure with sub-100 Pa detection limits and a response time of 90 ms is demonstrated. An embedded equivalent Wheatstone bridge circuit makes the most of tangential and radial strain fields, leading to high sensitivities of a 0.0835 kPa^{-1} change in output voltage. The Wheatstone bridge also provides temperature self-compensation, allowing for operation in the range of 20–50 °C. As examples of potential applications, a polydimethylsiloxane (PDMS) wristband with an embedded microfluidic diaphragm pressure sensor capable of real-time pulse monitoring and a PDMS glove with multiple embedded sensors to provide comprehensive tactile feedback of a human hand when touching or holding objects are demonstrated.

Keywords: diaphragm pressure sensors, flexible pressure sensors, liquid metal, microfluidics, wearable

INTRODUCTION

The development of flexible pressure sensors has various potential applications in soft robotics, wearable electronics, and artificial electronic skins.[1-15] For these applications, conventional rigid pressure sensors are unsuitable due to their fragility and low flexibility arising from their rigid material components. Over the years, various technologies have been proposed to enable flexible pressure sensing, such as utilizing elastomeric dielectric gate layers in thin film transistors[3, 15] or embedding conducting silver or carbon nanoparticles into an elastomer as a “pressure sensitive rubber”.[1, 10-12] Recently, a new approach utilizing the concept of “liquid-state electronics” has been proposed where conductive liquids are embedded into elastomer microchannels to form sensors.[16-23] Deformation of the elastomers contributes to changes in the cross-section areas and length of the microchannels, resulting in changes in resistance along the microchannels. Among many elastomers, polydimethylsiloxane (PDMS) has been the most explored due to its high elasticity and biocompatibility along with the ability to easily define sub-100 μm microchannels.

Due to high surface tension, high electrical conductivity, low toxicity, and low viscosity, Galinstan (a eutectic alloy of gallium, indium, and tin), and eutectic gallium-indium (EGaIn) have been the two most popular liquid metal alloys used for microfluidic sensors[22-27] or as substitutes for wires.[28-31] Approaches using such liquid metals are typically based on either multilayer capacitive force sensing[22] or resistive pressure sensing.[23] In addition to liquid metals, room temperature ionic-liquids have been used to build highly deformable nanogap capacitor-based pressure sensors at the liquid/solid interface[16] or resistive pressure sensing.[17]

In this paper, we report a microfluidic tactile sensor based on a diaphragm pressure sensor design. The diaphragm pressure sensor design utilizing an embedded equivalent Wheatstone bridge circuit makes the most of tangential and radial strain fields, allowing us to achieve a combination of high sensitivity, linearity, low limit of detection, high resolution, and temperature self-compensation. Key performance indicators are characterized to evaluate the diaphragm pressure sensor. Pulse sensing and tactile sensing using a smart wristband and glove are demonstrated as potential applications.

The diaphragm pressure sensor is designed and fabricated based on embedded Galinstan microchannels with 70 μm width and 70 μm height (Figure 1a). The fabrication process is described in the Experimental Section and Figure S1 in the Supporting Information. The pattern is composed of four primary sets of sensing grids. Two sets of tangential sensing grids are symmetrically located around diaphragm center and two sets of radial sensing grids are symmetrically located around diaphragm periphery. Four sets of sensing grids are connected end to end, with two nonadjacent terminals used for voltage input and the other two for voltage output, forming an equivalent Wheatstone bridge (Figure 1b,c). When uniform pressure is applied above the tangential sensing grids, tension around the

center causes a decrease in the microchannel cross-sectional area, leading to an increase in tangential bridge resistance (R_t). On the contrary, compression around the periphery results in an increase in microchannel cross-sectional area, hence a decrease in radial bridge resistance (R_r). The pattern design and the sensing mechanism are illustrated based on the theoretical strain distribution in a rigidly clamped diaphragm under uniform pressure (Figure S2, Supporting Information).[32, 33] Both tangential and radial strains are maximum and same at the diaphragm center, given by

$$\varepsilon_{r_c} = \varepsilon_{t_c} = \frac{3PR_0^2(1-\nu^2)}{8t^2E} \quad (1)$$

where P represents pressure applied on the contact area, R_0 is the diaphragm radius, t is diaphragm thickness, ν is Poisson's ratio, and E is the Young's modulus.

Figure 1. Microfluidic tactile diaphragm pressure sensor. a) Optical image of a finished microfluidic diaphragm sensor. b) Schematic layout of the diaphragm sensor and c) the equivalent circuit schematic forming an equivalent Wheatstone bridge circuit. d) Simulation of the normal stress for the radial sensing grids (σ_r) (along X-axis) and the normal stress for the tangential sensing grids (σ_t) (along Y-axis) of the sensor under 1 kPa pressure applied over a 9 mm diameter and e) a schematic diagram indicating testing conditions.

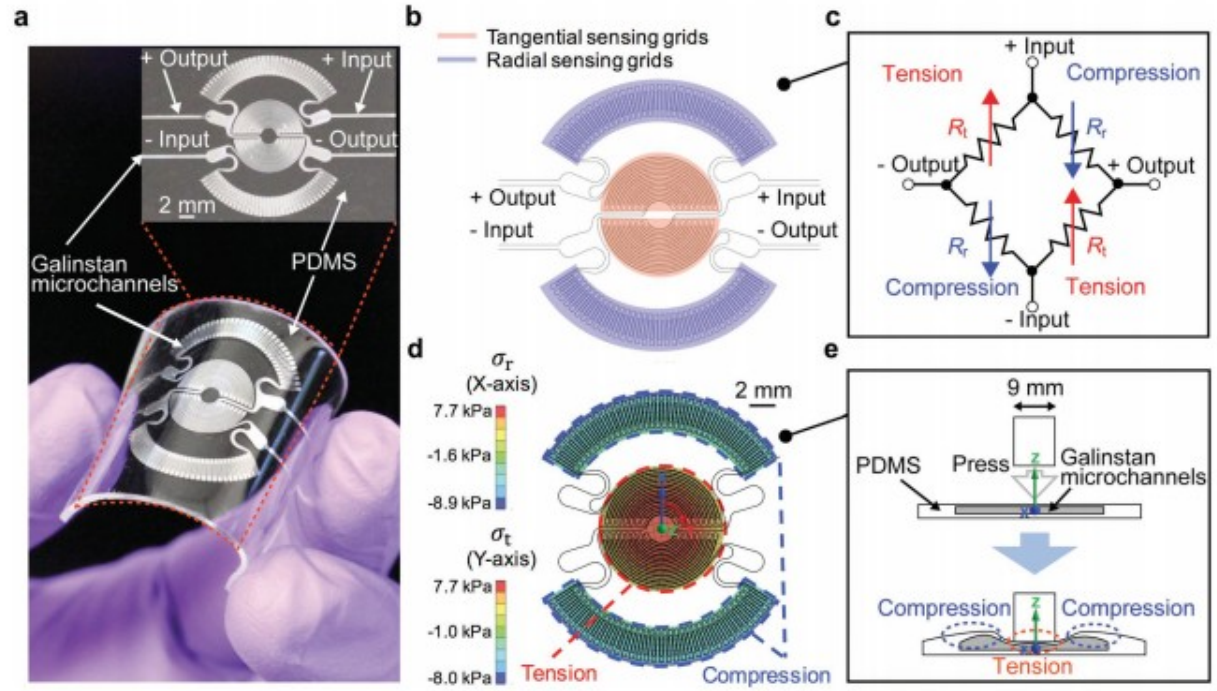

The tangential strain decreases away from the center until it reaches zero at the diaphragm periphery. Therefore:

$$\varepsilon_{r_0} = 0 \quad (2)$$

The radial strain decreases more rapidly than the tangential strain moving away from the center and becomes negative at diaphragm periphery, expressed by:

$$\varepsilon_{t_0} = -\frac{3PR_0^2(1-\nu^2)}{4t^2E} \quad (3)$$

The theoretical output voltage (V_{out}) of a diaphragm strain gage (assuming a gage factor of 2.0) for a given input voltage V_{in} is expressed approximately by[33]:

$$V_{out} = 0.75\frac{PR_0^2(1-\nu^2)}{t^2E}V_{in} \quad (4)$$

As can be seen, V_{out} is proportional to P by a constant factor when all the other parameters are fixed. It should be noted that equations in this work are based upon a series of assumptions.[33] In particular, the equations above assume an infinitely rigid clamping around the diaphragm periphery, which may lead to slight deviations as compared to our experimental device.

To better optimize our sensor, the optimal region on the diaphragm under which pressure is applied has to be calculated. Figure S3 in the Supporting Information compares normal stress (σ) simulations (using finite element method) along *X*-axis and *Y*-axis toward different diameter areas under which 1 kPa pressure is applied (20, 15, and 9 mm) for a sensor with a total diameter of 20 mm. Positive stress represents tension that occurs under the contact area, while negative stress means compression that occurs at the exterior (Figure 1e). As the area over which pressure is applied is decreased, a larger ratio of the compression region to tension region is gained. As can be seen in Figure 1d,e, the optimal area for pressure detection is a 9-mm-diameter circle for the explored sensor design.

In order to thoroughly characterize the performance of our microfluidic diaphragm sensor, a series of key performance indicators were identified and characterized. These indicators include sensitivity, linearity, detection limit, resolution, response time, repeatability, and thermal stability.[8] Sensitivity is defined as the relative change in voltage (ΔV) per unit of applied pressure with respect to the output voltage at zero pressure (V_0). Linearity is derived from the sensitivity regression line. The detection limit is defined as the minimum change in pressure that can be reliably detected above the noise floor. Resolution is the smallest amount of pressure change that can be accurately detected above the detection limit. The response time is characterized as the time from which pressure is applied to time at which the electrical output of the sensor reaches 90% of the steady state value. Thermal stability of the sensors is also important as the primary sensing mechanism of our sensor is resistance based, which can be affected by temperature fluctuations.

In order to characterize the diaphragm pressure sensor, a programmable displacement probe was used to apply static or dynamic pressure on the upper surface of the sensor. Meanwhile a commercial force sensor underneath was used to measure the applied force (Figure 2a). The experimental setup and protocol details are described in the Experimental Section. Figure 2b shows the real-time output voltage response of a sensor with a total diameter of 20 mm for five cycles of loading and unloading at various pressure levels, demonstrating the stability and repeatability of the sensor. Figure S4a in the Supporting Information shows a magnified graph of Cycle 5. The response time, derived from one step is 90 ms (Figure S4b, Supporting Information). Figure 2c plots the output voltage versus pressure under loading and unloading conditions. The loading and unloading sensitivities are 0.0835 and 0.0834 kPa^{-1}, respectively, with linearities of R^2 = 0.999 in both directions. Figure S4c in the Supporting Information illustrates the ability to detect subtle pressures with a detection limit of ≈98 Pa and resolution of less than 50 Pa. The error bars denote one standard deviation. It should be noted that the detection limit reported here is limited due to the measurement setup, and the true detection limit of the system is most likely lower. The diaphragm pressure sensor is able to operate up to pressures of ≈0.8 MPa before failure. The tangential and the radial bridges are designed to be almost the same resistance, with the tangential resistance 5% above the radial one (to guarantee a consistent positive output voltage). As such, the equivalent Wheatstone bridge design eliminates fluctuations in output voltage due to temperature variation, providing temperature self-compensation without requiring any external calibration. This is demonstrated in Figure 2d where a 0.07% change in sensitivity per °C is seen in the temperature range of 20–50 °C. Table S1 in the Supporting Information illustrates a comparison between the diaphragm pressure sensor and other conductive liquid-based pressure sensors. As can be seen, our diaphragm sensor design shows the lowest limit of detection and response time at 98 Pa and 90 ms, respectively, while maintaining sensitivities and linearities on par with other reports.

Figure 2. Assessment of the diaphragm pressure sensor. a) Optical image of the experimental setup used for testing. b) Real-time monitoring of the output voltage change as the pressure is stepped up and down over five cycles. c) Calibration of the output voltage versus pressure of the diaphragm pressure sensor under loading and unloading conditions. d) Effect of temperature on the output voltage at various temperatures and pressures.

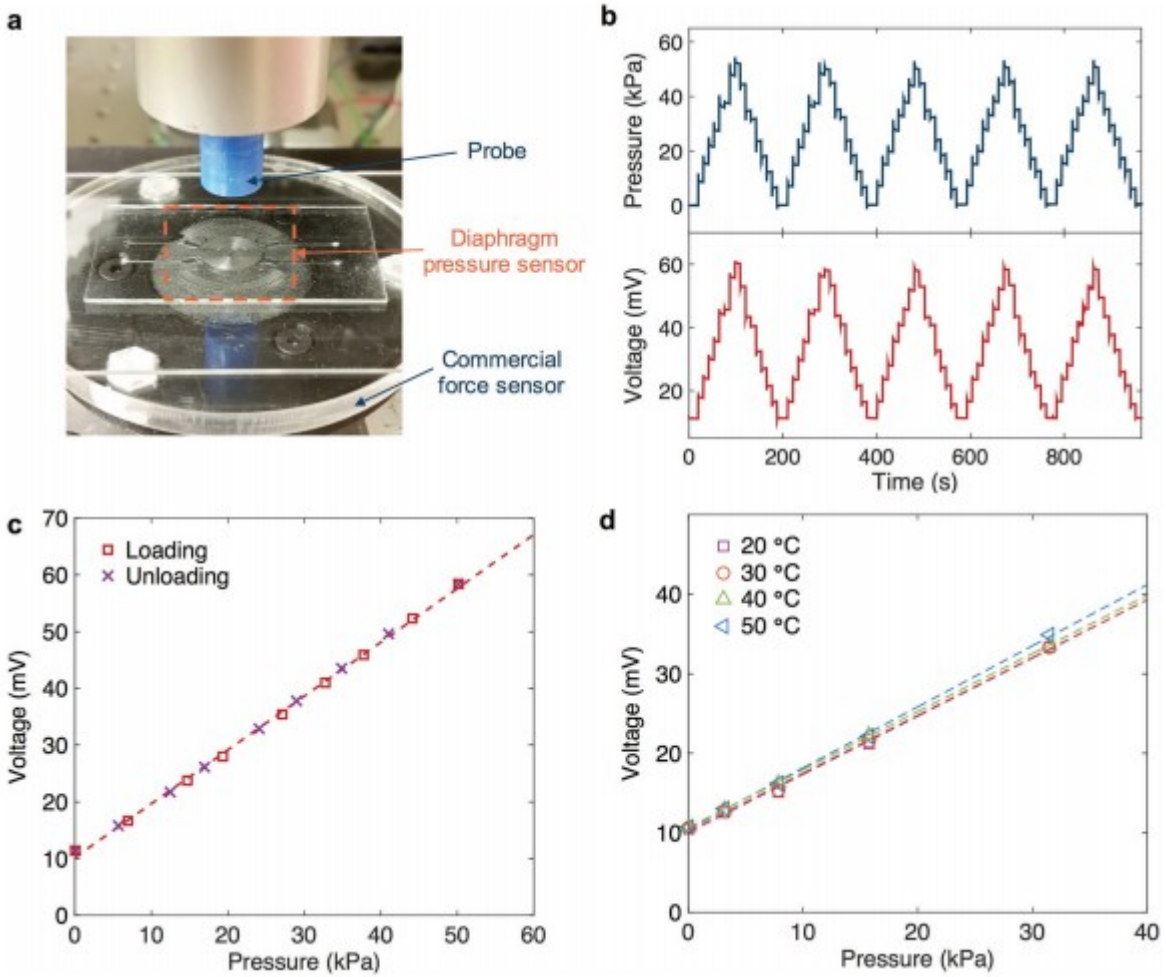

As different applications may require sensing pressure applied over different sized areas, four sensors with diameters of 1.8, 10, 15, and 20 mm (Figure 3a) were designed and fabricated to observe the effect of dimension on sensitivity. Notably, the patterns with 15, 10, and 1.8 mm diameters were not simply rescaled from the 20 mm pattern as the microchannel cross-section (70 µm width × 70 µm height) of the 20 mm sensor were already at a minimum at which reliable fabrication could be done. Given this, the 15, 9, and 1.8 mm sensors were modified to have the same microchannel cross-section dimensions as the 20 mm sensor.

Figure 3. Effect of sensor size. a) Optical image of four different sensors with diameters of 20, 15, 10, and 1.8 mm with a penny for size reference. b) The relative output voltage change versus pressure for the four different sized sensors. c) Plot of the sensitivity versus sensor size compared to theoretical simulations.

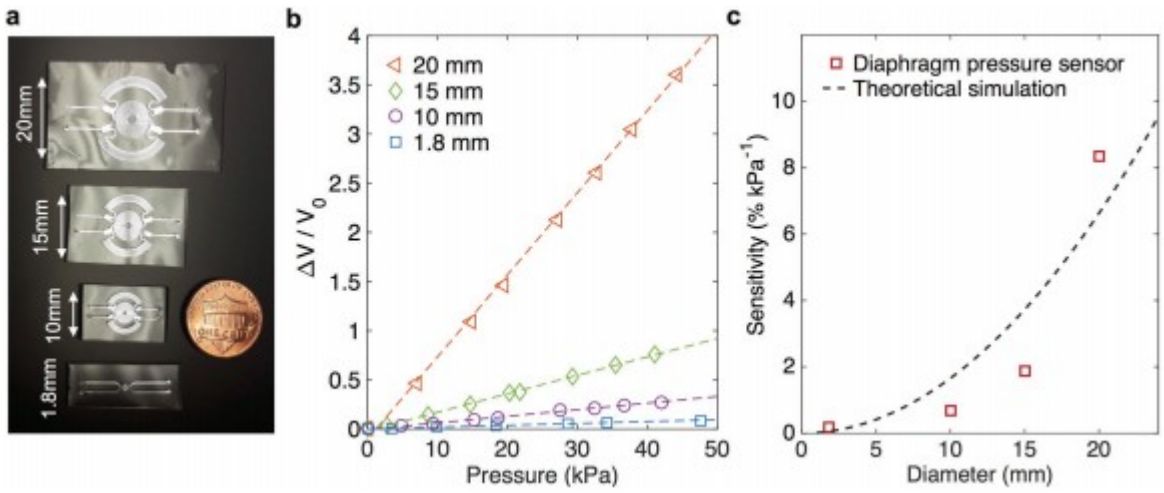

Figure 3b demonstrates a comparison of $\Delta V/V_0$ versus pressure for the different sized sensors (Figure S5, Supporting Information, shows the absolute voltage changes). All measurements were taken at an operating voltage of 30 mV. Figure 3c shows the dependence of sensitivity (kPa^{-1}) on the sensor diameters. The relationship between sensitivity and radius R_0 derived from Equation 4 is plotted in Figure 3c as theoretical reference. As expected, the sensitivity increases approximately quadratically with sensor diameter. However, for many applications where the contact area is small or where spatial mapping is required, smaller sensor diameters may be more appropriate despite lower sensitivities.

Due to its performance, our diaphragm pressure sensor meets the requirement of a variety of potential applications. Among many, one feasible and effective health monitoring application is heart-rate monitoring. As a proof of concept, a PDMS wristband with an embedded microfluidic diaphragm pressure sensor was designed and fabricated to measure dynamic pulse measurements. To test the sensor, the PDMS wristband was worn directly on a subject's (Subject A) wrist, with the sensor located at the position of the radial artery, during cycling (Figure 4a–c). Subject A's pulse was first recorded in a stationary state for 2 min followed by 2 min of exercise at 100, 200, and 300 W each on a cycling ergometer. A commercial TICKR heart rate monitor (Wahoo fitness) was worn by Subject A during the entire process for comparison. Figure 4e exhibits the smoothed pulse result (in beat per min (bpm)) using time intervals between adjacent pulse peaks along with results from the commercial monitor. The raw data and code used for smoothing can be found in Figure S6 and File S1 in the Supporting Information, respectively. The initial pulse rate of Subject A was around 75–80 bpm which then rapidly increased after the start of cycling. Subject A's pulse continued to increase with increasing exercise power and reached a maximum of 137 bpm at 8 min after which cycling ended. It then dropped down to almost the initial level after a period of rest. As can be seen in Figure 4e, the diaphragm pressure sensor data are very similar to the output

of the commercial monitor. Figure 4f,g shows the real time output voltage measurements over 10 s periods during rest and at peak pulse rate, respectively. Furthermore, there is also a difference in the magnitude of output voltage change which corresponds to differences in the strength of the heart beats arising from the exercise.

Figure 4. Heart-rate monitoring. a) Optical image of a subject wearing the PDMS sensor wristband on a cycling ergometer. b) Schematic and c) optical image of how the sensor is worn for measurements. d) Optical image of the 1.8 mm sensor used. e) Plot of the pulse rate measured by the sensor and a commercial reference monitor during exercise. f) Real time measurement data over a 10 s span taken during rest and g) at peak pulse rate.

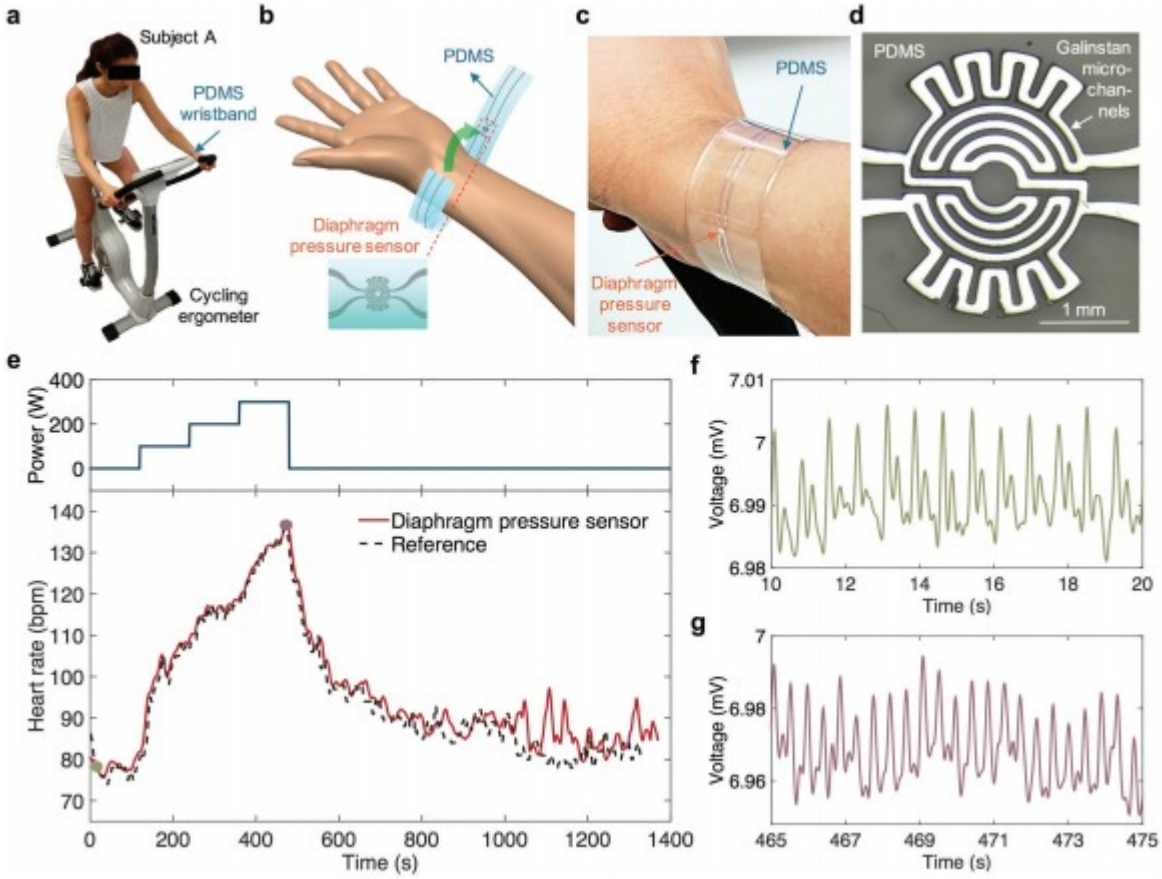

In addition to the low detection limit and high resolution, the broad detection range of the diaphragm pressure sensor makes it a promising candidate for tactile pressure sensing. As a demonstration, a PDMS “smart glove” with multiple embedded microfluidic diaphragm pressure sensors (Figure 5a,b) was designed and fabricated via 3D printed hand molds (Figure S7, Supporting Information, and the Experimental Section). Seventeen diaphragm pressure sensors are embedded within the smart glove, 10 on the fingers and 7 on the palm, allowing for comprehensive tactile sensing when touching or holding objects. The smart glove is capable of providing dynamic responses toward a variety of hand motions such as holding, gripping,

grasping, squeezing, lifting, moving or touching objects. As an example, Figure 5c,d shows the real-time response recorded from the corresponding thumb and index finger sensors for a subject (Subject B) gently grasping and releasing a grape. As can be seen, the outputs of both sensors increase simultaneously at the moment of touching and returned to initial values after release. Figure 5e shows Subject B gripping a bat, with the inset depicting a color intensity map of the relative voltage change ($\Delta V/V_0$) sent back from the corresponding sensors on the entire hand, indicating the distribution of contact pressure. This example of a spatially resolved, pressure sensitive glove could be used to provide haptic feedback for potential applications in virtual/augmented reality interactive environments, robotics, and remote healthcare.

Figure 5. Tactile sensing glove. a) Photograph of hand-shaking wearing the PDMS tactile sensing glove. b) Schematic of the PDMS tactile sensing glove. c) Photograph of the tactile sensing glove worn while grasping a grape. d) Real-time response recorded from the corresponding thumb and index finger sensors for gently grasping and releasing the grape. e) Photograph of the tactile sensing glove worn while gripping a bat and the corresponding output voltage map across the sensors within the glove.

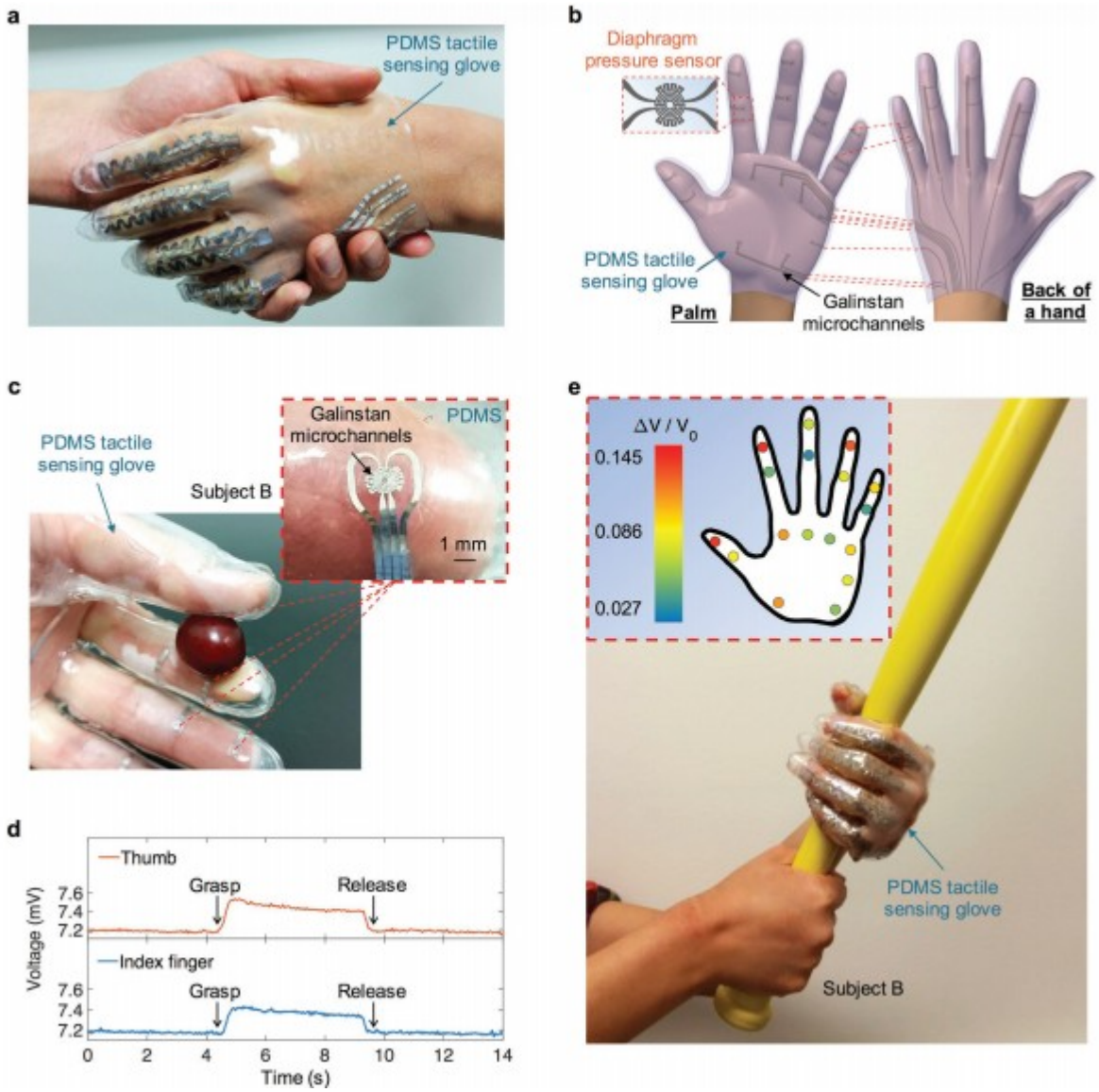

In this paper, a microfluidic tactile diaphragm pressure sensor based on embedded Galinstan microchannels was developed. By using an embedded equivalent Wheatstone bridge circuit to take advantage of the tangential and radial strain fields, sensitivities as high as 0.0835 kPa^{-1} with high response linearity could be achieved. The usage of the Wheatstone bridge design also provides built-in temperature compensation allowing for operation between 20 and 50 °C without external offsets. The detection limit of our sensor has been shown to be below 100 Pa with sub-50 Pa resolution. The extremely low detection limit and resolution combined with an ultrafast response time of 90 ms allows for the sensor to be used in a wide range of applications. A PDMS wristband with an embedded microfluidic diaphragm pressure sensor illustrates the extraordinary performance of the sensor to detect and monitor heart rate from the wrist pulse. A PDMS smart glove with multiple embedded microfluidic diaphragm pressure sensors provides comprehensive and effective tactile mapping of the human hand when touching or holding

objects. As demonstrated, the liquid-state diaphragm pressure sensors may be utilized as either standalone devices for monitoring pressure at a specific point or into large arrays for tactile mapping in a variety of electronic skin and smart textile applications for wearables, robotics, and beyond.

Experimental Section

Materials: Dow Corning Sylgard 184 Silicone Elastomer Clear was purchased from Ellsworth Adhesives (Germantown, WI). Low Melting Point −2 F Alloy Eutectic Gall/Indium (Galinstan) was purchased from Rotometals, Inc. (San Leandro, CA). SU-8 2075 and propylene glycol monomethyl ether acetate were purchased from MicroChem Corp. (Newton, MA). Trichloro (1H,1H,2H,2H-perfluorooctyl) silane (PFOTS) 97% was purchased from Sigma-Aldrich Co. (St. Louis, MO). Dow Corning 734 Clear Flowable Plus Silicone Sealant was purchased from Styles Logistics, Inc. (LaGrangeville, NY). All reagents were used as received.

Fabrication of SU-8 Mold: A bare silicon wafer (4 or 6 in.) was spin coated with SU-8 photoresist (10 s at 500 rpm, ramped at 50 rpm s^{-1} to 3000 rpm for 30 s) and then put through soft baking (65 °C for 5 min and then 95 °C for 25 min). Once cooled down, the SU-8 wafer was exposed using a transparency mask with the diaphragm pressure sensor pattern. Then the SU-8 wafer was put through a post exposure bake (65 °C for 5 min and then 95 °C for 10 min) followed by development in propylene glycol monomethyl ether acetate (SU-8 developer).

Fabrication of Microfluidic Tactile Diaphragm Pressure Sensors: The SU-8 mold was exposed to oxygen plasma at 120 W for 2 min and then treated with trichloro PFOTS to form an antiadhesive layer allowing for cured PDMS to more easily detach. A PFOTS doseage of 40 µL per 4 in. wafer and 90 µL per 6 in. wafer was used for the treatment, conducted using a vacuum for 1 h. Dow Corning Sylgard 184 Silicone Elastomer Clear was mixed at a 10:1 ratio to make liquid PDMS. The liquid PDMS was placed in a vacuum dessicator for 30 min to remove air bubbles and subsequently spin coated onto the SU-8 mold at 500 rpm for 30 s to form an ultrathin PDMS membrane with a thickness of ≈170 µm (Figure S2a,b, Supporting Information). The liquid PDMS membrane was then cured at 70 °C for 1 h. Another plain PDMS membrane was fabricated in similar ways except that the liquid PDMS was spin coated onto an unpatterned glass slide (Figure S2c,d, Supporting Information). The patterned PDMS membrane from the SU-8 mold and the plain PDMS membrane were then exposed to oxygen plasma at 90 W power for 90 s and then permanently bonded together at 70 °C for 15 min (Figure S2e, Supporting Information). Subsequently, Galinstan was injected into the microchannels (Figure S2f, Supporting Information) and the inlets and outlets were sealed using Dow Corning 734 Clear Flowable Plus Silicone Sealant with exterior connection wires.

Experimental Set Up for Static and Dynamic Measurements: Static and dynamic measurements were performed using a three-axis force-

displacement testing station.[34] The testing station employs three stepper motors (Zaber LSQ075A-E01 and T-LSR150B) that are driven by a stepper motor controller (Galil DMC-4143) running in an open-loop control configuration. Loading profiles were coded in G-code and run in Mach3, which interfaces with the motor controller.

The diaphragm pressure sensor was placed on a glass slide that was in turn anchored to a six-axis force-torque sensor (ATI Nano43) mounted on the *XY*-stage. A customized 3D-printed cylindrical probe (9 mm diameter) was mounted on the *Z*-stage, aligned over the sensor's sensing pattern and the flat end was pressed into the sensor at discrete loading forces (0–3 N) to characterize the sensor, by first characterizing the stiffness of the sensor and then compressing the sensor appropriate distances with the probe. In each cycle of Figure 2b, the probe was coded to gradually step down to several certain positions with a 10 s pause before gradually stepping up. The loading/unloading speed is 12 μm s^{-1}.

The sensor loading force applied by the probe was measured using the force-torque sensor. The sensor's response was measured by applying 1 V across the bridge input nodes, and measuring the voltage across the bridge output nodes. The output voltage was then amplified by 40× with a noninverting operational amplifier circuit. The amplified sensor voltage and the loading force were logged with a Data Acquisition (DAQ) (NI USB 6259) and filtered with a low-pass filter (4th-order Butterworth filter at 40 Hz) prior to analysis.

Fabrication of PDMS Tactile Sensing Gloves: The fabrication process is exhibited in Figure 5b and Figure S7 in the Supporting Information. Customized 3D printed acrylonitrile butadiene styrene (ABS) hand mold and shell molds were first smoothened using acetone so that the PDMS part of the glove would be transparent. Customized PDMS membranes fabricated separately beforehand with embedded sensors and connections layout for the thumb, index finger, middle finger, ring finger, little finger, and palm were placed between the hand and shell molds in their respective positions. The shell molds were then closed, and the liquid PDMS was poured into the mold to form the glove. The whole mold was cured for 2 h at 50 °C in a vacuum oven after which the finished PDMS glove could be easily detached from the molds using hand soap and water.

Acknowledgements

Y.G. and H.O. contributed equally to this work. This work was supported by the National Science Foundation (NSF) NASCENT Center. Y.G. acknowledges support from the China Scholarship Council (File No. 201406250097). H.O. acknowledges support from the Japan Society for the Promotion of Science (JSPS) Fellowship. H.O. acknowledges support from the JSPS Fellowship and Grant-in-Aid for Young Scientists (A). K.C. acknowledges support from the Robert Noyce Memorial Fellowship in Microelectronics. The authors thank James Bullock, Minghan Chao, Ziba Shahpar, Carlos Casarez, Matin Amani, Der-Hsien Lien, Colleen Forney, and Shyam Patel in University of California,

Berkeley, and staff in SUPERNODE of University of California, Berkeley for their help.

Conflict of Interest

The authors declare no conflict of interest.

REFERENCES

1. C. Wang, D. Hwang, Z. Yu, K. Takei, J. Park, T. Chen, B. Ma, A. Javey, *Nat. Mater.* 2013, 12, 899.

2. Y.-L. Tai, Z.-G. Yang, *J. Mater. Chem. B* 2015, 3, 5436.

3. G. Schwartz, B. C.-K. Tee, J. Mei, A. L. Appleton, D. H. Kim, H. Wang, Z. Bao, *Nat. Commun.* 2013, 4, 1859.

4. L. Y. Chen, B. C.-K. Tee, A. L. Chortos, G. Schwartz, V. Tse, D. J. Lipomi, H.-S. P. Wong, M. V. McConnell, Z. Bao, *Nat. Commun.* 2014, 5, 5028.

5. Y. Shu, C. Li, Z. Wang, W. Mi, Y. Li, T.-L. Ren, *Sensors* 2015, 15, 3224.

6. S. Stassi, V. Cauda, G. Canavese, C. Pirri, *Sensors* 2014, 14, 5296.

7. F. Zhang, Y. Zang, D. Huang, C. Di, D. Zhu, *Nat. Commun.* 2015, 6, 8356.

8. Y. Zang, F. Zhang, C. Di, D. Zhu, *Mater. Horiz.* 2015, 2, 140.

9. L. Pan, A. Chortos, G. Yu, Y. Wang, S. Isaacson, R. Allen, Y. Shi, R. Dauskardt, Z. Bao, *Nat. Commun.* 2014, 5, 3002.

10. S. Lee, A. Reuveny, J. Reeder, S. Lee, H. Jin, Q. Liu, T. Yokota, T. Sekitani, T. Isoyama, Y. Abe, Z. Suo, T. Someya, *Nat. Nanotechnol.* 2016, 11, 472.

11. D. J. Lipomi, M. Vosgueritchian, B. C.-K. Tee, S. L. Hellstrom, J. A. Lee, C. H. Fox, Z. Bao, *Nat. Nanotechnol.* 2011, 6, 788.

12. Y. Joo, J. Byun, N. Seong, J. Ha, H. Kim, S. Kim, T. Kim, H. Im, D. Kim, Y. Hong, *Nanoscale* 2015, 7, 6208.

13. S.-J. Woo, J.-H. Kong, D.-G. Kim, J.-M. Kim, *J. Mater. Chem. C* 2014, 2, 4415.

14. T. Li, H. Luo, L. Qin, X. Wang, Z. Xiong, H. Ding, Y. Gu, Z. Liu, T. Zhang, *Small* 2016, 12, 5042.

15. S. C. B. Mannsfeld, B. C.-K. Tee, R. M. Stoltenberg, C. V. H.-H. Chen, S. Barman, B. V. O. Muir, A. N. Sokolov, C. Reese, Z. Bao, *Nat. Mater.* 2010, 9, 859.

16. J. Yan, *J. Micro/Nanolithogr., MEMS, MOEMS* 2012, 11, 13005.

17. C.-H. Lin, C.-K. Wang, Y.-A. Chen, C.-C. Peng, W.-H. Liao, Y.-C. Tung, *Sci. Rep.* 2016, 6, 36425.

18. J. C. Yeo, J. Yu, Z. M. Koh, Z. Wang, C. T. Lim, *Lab Chip* 2016, 16, 3244.

19. J. C. Yeo, Kenry, J. Yu, K. P. Loh, Z. Wang, C. T. Lim, *ACS Sens.* 2016, 1, 543.

20. Y.-L. Park, B.-R. Chen, R. J. Wood, *IEEE Sens. J.* 2012, 12, 2711.

21. D. M. Vogt, Y.-L. Park, R. J. Wood, *IEEE Sens. J.* 2013, 13, 4056.

22. R. D. Ponce Wong, J. D. Posner, V. J. Santos, *Sens. Actuators, A* 2012, 179, 62.

23. T. Jung, S. Yang, *Sensors* 2015, 15, 11823.

24. H. Ota, K. Chen, Y. Lin, D. Kiriya, H. Shiraki, Z. Yu, T.-J. Ha, A. Javey, *Nat. Commun.* 2014, 5, 5032.

25. T. Liu, P. Sen, C.-J. Kim, *J. Microelectromech. Syst.* 2012, 21, 443.

26. H. Ota, S. Emaminejad, Y. Gao, A. Zhao, E. Wu, S. Challa, K. Chen, H. M. Fahad, A. K. Jha, D. Kiriya, W. Gao, H. Shiraki, K. Morioka, A. R. Ferguson, K. E. Healy, R. W. Davis, A. Javey, *Adv. Mater. Technol.* 2016, 1, 1600013.

27. H.-S. Shin, J. Ryu, C. Majidi, Y.-L. Park, *J. Micromech. Microeng.* 2016, 26, 25011.

28. S. Cheng, *Advanced Elastomers: Technology, Properties, and Application* (Ed: A. Boczkowska), InTech, Croatia, 2012.

29. G. Li, X. Wu, D.-W. Lee, *Sens. Actuators, B* 2015, 221, 1114.

30. H. Hu, K. Shaikh, C. Liu, *IEEE Sens.* 2007, 815.

31. M. D. Dickey, R. C. Chiechi, R. J. Larsen, E. A. Weiss, D. A. Weitz, G. M. Whitesides, *Adv. Funct. Mater.* 2008, 18, 1097.

32. W. P. Eaton, J. H. Smith, *Smart Mater. Struct.* 1997, 6, 530.

33. Micro-Measurements, Vishay Precision Group, Design consideration for diaphragm pressure transducers, 2003.

34. A. G. Gillies, R. S. Fearing, *Langmuir* 2011, 27, 11278.